

# Simulations of rotating neutron star collapse with the puncture gauge: End state and gravitational waveforms

Tim Dietrich<sup>1</sup>, Sebastiano Bernuzzi<sup>2,3</sup>

<sup>1</sup>*Theoretical Physics Institute, University of Jena, 07743 Jena, Germany*

<sup>2</sup>*TAPIR, California Institute of Technology, 1200 East California Boulevard, Pasadena, California 91125, USA and*

<sup>3</sup>*DiFeST, University of Parma, I-43124 Parma, Italy*

(Dated: June 24, 2015)

We reexamine the gravitational collapse of rotating neutron stars to black holes by new 3+1 numerical relativity simulations employing the Z4c formulation of Einstein equations, the moving puncture gauge conditions, and a conservative mesh refinement scheme for the general relativistic hydrodynamics. The end state of the collapse is compared to the vacuum spacetime resulting from the evolution of spinning puncture initial data. Using a local analysis for the metric fields, we demonstrate that the two spacetimes actually agree. Gravitational waveforms are analyzed in some detail. We connect the emission of radiation to the collapse dynamics using simplified spacetime diagrams, and discuss the similarity of the waveform structure with the one of black hole perturbation theory.

PACS numbers: 04.25.D-, 04.30.Db, 95.30.Sf, 97.60.Jd

## I. INTRODUCTION

A fundamental problem in general and numerical relativity is the simulation of the gravitational collapse of a rotating neutron star to a black hole. The problem is of theoretical and astrophysical relevance, and it has been studied in some detail by means of two-dimensional axisymmetric simulations [1–7] and three-dimensional simulations [8–13]. The relevant theoretical questions are related to the nature of the collapse spacetime, black hole formation and its properties. Astrophysically, rotating neutron stars close to the collapse threshold can be produced in stellar core collapse or neutron star mergers, e.g. [14, 15]. Associated to such events, a significant emission of electromagnetic, neutrino and gravitational radiation is expected, e.g. [16]. Accurate numerical relativity simulations are essential to develop emission models. Thus, understanding the technical details of the simulations, such as the role of the gauge and the sources of inaccuracies, is of particular importance. In this paper we reexamine two key aspects of the rotating collapse by a new set of numerical relativity simulations.

First, we investigate the end state of the collapsing spacetime when puncture gauge conditions are adopted, and compare it to the spacetime of a single spinning puncture. Gauge conditions are a key technical point for the simulation of collapse in 3+1 general relativity. The combination of the 1+log slicing condition [17] and Gamma-driver shift for the spatial gauge [18, 19], commonly referred as “puncture gauge” [65], allows one to perform stable simulations and follow black hole formation without excision treatment [22]. A clear understanding of the role of this gauge in the gravitational collapse scenario has been achieved only in the spherically symmetric case [23]. For axisymmetric spacetimes little is known. In vacuum, it is unclear how and to what stationary slice of Kerr the conformally flat spinning puncture initial data evolve. Some numerical and analytical

studies have recently been performed in [24, 25]. Here, we present the first analysis in presence of matter.

Second, we calculate the gravitational waveforms (GWs) emitted during collapse. Consistent gravitational waveforms from the neutron star collapse can be computed only using full general relativity. It has been pointed out long ago, and notably in [1, 26–28], that the relevant features are rather simple and waveforms resemble the ones generated by a particle infalling the black hole [2, 29]. However, several three-dimensional studies suggest a more complicated wave pattern with the exception of recent work of [13] (see also [30]) in which the “perturbative picture” holds. Our data confirm the latter result. The investigation of these aspects requires very precise numerical data. In this work, such precision is achieved by the use of (i) a conservative mesh refinement scheme for the hydrodynamics evolution [13, 31, 32], and (ii) the Z4c formulation of Einstein equations [33], which is applied for the first time to this problem.

The paper is organized as follows. Section II summarizes the equations, the numerical method, and the implementation details. Section III presents the dynamics of the gravitational collapse. Section IV compares our numerical results with the spacetime of a spinning puncture. Section V focuses on the emitted gravitational waves. We conclude in Sec. VI. Throughout the article dimensionless units are used, i.e. we set  $c = G = M_{\odot} = 1$ .

## II. METHOD

### A. Numerical relativity framework

Let us start discussing briefly the general relativity framework employed in this work. Einstein’s field equations are written in 3+1 form and formulated as the Z4c system [33, 34]. The gauge conditions are specified as evolution equations for the lapse function  $\alpha$  and the shift

vector  $\beta^i$ . We employ the 1+log slicing condition [17],

$$\partial_t \alpha = \beta^i \partial_i \alpha - \alpha^2 \mu_L \hat{K}, \quad (1)$$

together with the integrated version of the Gamma-driver shift condition [18, 19]

$$\partial_t \beta^i = \mu_S \Gamma^i - \eta \beta^i + \beta^j \partial_j \beta^i. \quad (2)$$

Above,  $\hat{K}$  is the trace of the extrinsic curvature in the Z4c formulation and  $\Gamma^i$  the conformal connection functions. These conditions are commonly referred to as “puncture gauge”. Puncture gauge conditions have been proved to be a key element for collapse simulations [22, 23]. The gauge parameters in Eqs. (1)-(2) are chosen as  $\eta = 0.3$ ,  $\mu_L = 2/\alpha$ , and  $\mu_S = 1$ . We employ the constraint damping scheme of the Z4c formulation, and set the damping parameters to  $\kappa_1 = 0.02$  and  $\kappa_2 = 0$  [35].

The neutron star matter is described within general relativistic hydrodynamics (GRHD) [36]. Eulerian GRHD equations are written in conservative form and coupled with the evolution equations for the spacetime. We use the same notation and equations as described in [15], and refer to that paper for details. The equation of state for the fluid considered here is the  $\Gamma$ -law,

$$p = (\Gamma - 1)\rho\epsilon, \quad (3)$$

where  $p$  is the fluid pressure,  $\rho$  the rest-mass density,  $\epsilon$  the specific internal energy, and  $\Gamma$  the adiabatic exponent.

### B. BAM code

For our simulations we use the BAM code described in [15, 37]. The numerical method is based on the method of lines, Cartesian grids and finite differencing. BAM implements a grid made of a hierarchy of cell-centered nested Cartesian boxes. The grid structure is build out of  $L$  levels of refinement labeled  $l = 0, \dots, L - 1$ . Every refinement level  $l$  has one or more Cartesian grids with constant grid spacing  $h_l$  and  $n$  points per direction. Levels are typically refined in resolutions of constant factors of two. Levels with  $l > l_m$  can employ a different number of points per direction,  $n_m \neq n$ . Runge-Kutta type integrators are used for the time evolution. For the time stepping the Berger-Oliger algorithm (BO) is employed [38]. Metric spatial derivatives are approximated by fourth-order finite differences. GRHD equations are solved with a standard high-resolution-shock-capturing scheme based on primitive reconstruction and the Local-Lax-Friedrich central scheme for the numerical fluxes. Primitive reconstruction is performed with the fifth-order weighted essentially non-oscillatory (WENO) scheme of [39] (see [40] for its application in numerical relativity).

The main difference with respect to previous work is the implementation of an algorithm to enforce mass conservation of the hydrodynamical quantities among different refinement levels [31] (see also [13, 32] for numerical relativity implementations). This algorithm allows

TABLE I: Grid configurations for the BAM simulations:  $L$  number of total levels,  $n$  number of points per direction,  $L_m$  number levels employing  $n_m$  points per direction (every level  $l > 3$ ),  $h_f$  finest grid spacing,  $h_c$  coarsest grid spacing. The neutron star is covered completely by level  $l = 5$ , while its equatorial radius is  $\sim 7.7M_\odot$ . The outer boundary is roughly at  $r_{\text{out}} \sim 576M_\odot$ .

Name	$L$	$n$	$L_m$	$n_m$	$h_f$	$h_c$
G8	8	144	4	64	0.0625	8
G9L	9	108	5	48	0.04167	10.67
G9	9	144	5	64	0.03125	8
G9H	9	216	5	80	0.025	6.4
G10	10	144	6	64	0.015625	8
G11	11	144	7	64	0.0078125	8
G11H	11	216	7	96	0.0052083	5.33
G11F	11	288	7	128	0.00390625	4

us to use refinement levels inside the neutron star without introducing mass violation. Our implementation follows [32]; details and extensive tests for single and binary neutron star spacetimes will be given elsewhere [41]. We mention that, throughout this work, we use averages for the BO restriction and a second-order ENO (essentially non-oscillatory) scheme for the BO prolongation step.

Simulations presented in this work employ quadrant symmetry. The grid configurations are described in Table I. We investigate numerical uncertainties by increasing both the number of refinement levels keeping the same number of points per directions, and the resolution for a fixed number of levels. The former procedure allows us to better resolve the origin and the puncture in an efficient way; the latter has usually a larger effect on the waveforms. In the next sections these effects are discussed.

### III. COLLAPSE DYNAMICS

We study the rotational collapse by evolving a particular initial stellar configuration constructed by perturbing a uniformly rotating neutron star model in unstable equilibrium, i.e. beyond the radial stability point. In this section we describe the dynamics of the collapse and the grid/resolution dependence in our simulations.

The initial data configuration is the D4 model investigated previously in [10, 11, 13, 30]. This choice facilitates the comparison with previous work. The equation of state is a  $\Gamma = 2$  polytrope  $p = K\rho^\Gamma$  with  $K = K_{\text{ID}} = 100$ , the model’s central rest-mass density is  $\rho_c = 4.0869 \cdot 10^{-3}$ , the axes ratio is 0.65, the gravitational mass  $M = 1.8605M_\odot$ , and the baryonic mass  $M_b = 2.0443M_\odot$ . The equilibrium configuration has been computed with Stergioulas’s RNS code [42].

The gravitational collapse can be induced either by a pressure perturbation or by computing initial data at low resolution. Both methods violate Einstein constraints;

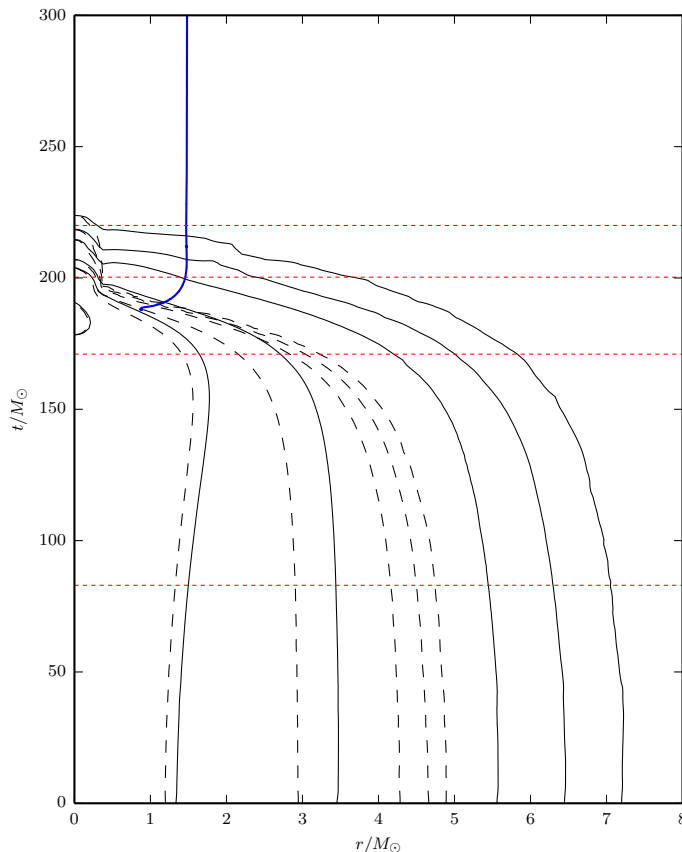


FIG. 1: Spacetime diagram visualizing the collapse dynamics of G11H. Contour lines in the equatorial plane (black solid) and perpendicular plane (black dashed) are shown for  $\rho = 2.5 \cdot 10^{-5}, 10^{-4}, 2.5 \cdot 10^{-4}, 10^{-3}, 2.5 \cdot 10^{-3}, 10^{-2}$ . The apparent horizon forms at  $188M_\odot$  (straight blue line). Red dashed horizontal lines correspond to special features of in the gravitational wave signal as marked in Fig. 9.

the violation can affect significantly the calculation of gravitational radiation. For large perturbations or low-resolution initial data we observe a large unphysical burst of radiation at early times; in some cases this burst has an amplitude comparable to the waveform amplitude and cannot be clearly separated from the physical data. We minimize this effect by choosing a small perturbation and using high resolutions. Specifically, we reduce the initial pressure of 0.5% by recomputing its equilibrium value with a different polytropic constant,  $K = 99.5$ , then the unperturbed one  $K_{\text{ID}} = 100$  (compare with [10, 11, 13] where 2% and [30] where 0.1% was applied). The model is then evolved with Eq. (3).

The collapse dynamics is summarized by the simplified spacetime diagrams shown in Fig. 1, which shows the evolution of the coordinate star surface, constant density lines, and apparent horizon radius; see e.g. [10]. Most of the matter contracts in an almost homologous way and maintains its axisymmetric distribution until  $t \sim 175M_\odot$ . Notice, however, that at high densities ( $r \lesssim 2$ ) the con-

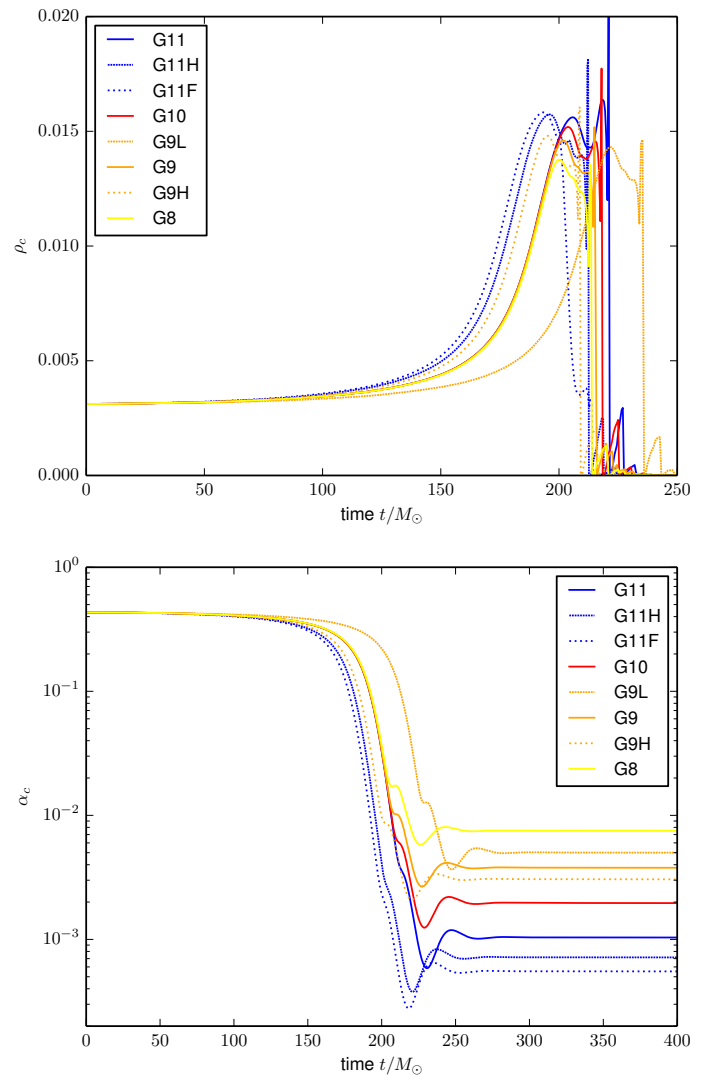


FIG. 2: Rotating collapse central dynamics. Central rest-mass density (top) and central lapse (bottom). Results for various grid configurations and resolution are shown.

tour lines slightly expand before collapsing. An apparent horizon is first found at  $t \sim 188M_\odot$  (for resolution G11H). Soon after horizon formation, all the matter is inside the horizon and actually “falls off” the grid due to gauge conditions (see [23] and below). In Sec. V we will further discuss this spacetime diagram, and identify specific waveform features for each time marked in Fig. 1.

Figure 2 shows the evolutions of the central (coordinate radius  $r \approx 0$ ) density  $\rho_c$  and the central lapse  $\alpha_c$ . During collapse the central lapse decreases and the central density increases; the latter reaches a maximum at  $t \sim 195M_\odot$ . The plot shows results for different grid configurations. By increasing the number of refinement levels the origin is better resolved, and consequently the maximum density (lapse) increases (decreases). Notice this is consistent with the argument of [23]. By varying

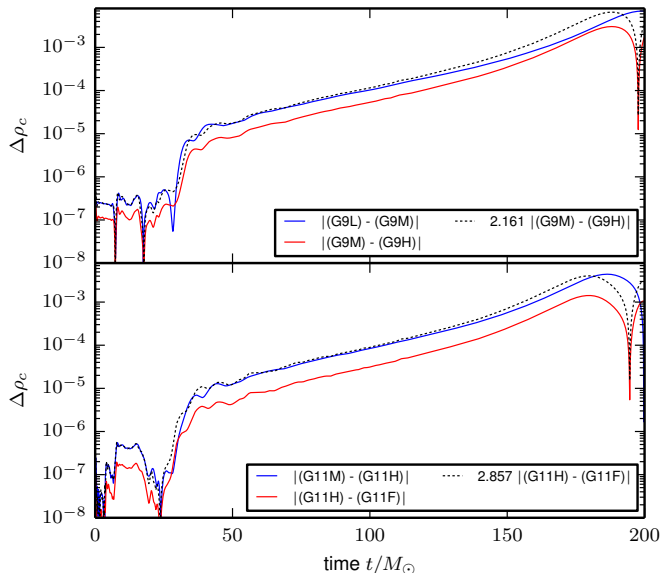


FIG. 3: Convergence test for the density  $\rho_c$  for the G9 (upper panel) and G11 (lower panel) grid configurations. For both triplets the results scale at approximately second order; convergence is more robust and observed longer for the higher resolved G11 data.

the resolution for a given grid setup we observe a monotonic behavior. The resolution effect (see the dashed-solid-dotted lines for configurations G9 and G11) can be as large as the effect of including more refinement levels; hence both parameters need to be tuned for an optimal grid setup. For higher resolutions the collapse happens earlier.

In Fig. 3 we show a standard three-level self-convergence plot for the central density  $\rho_c(t)$ . Similar plots are also obtained for other quantities. For the G11 configurations we observe second-order convergence almost up to horizon formation (see later), while for G9 convergence is slower after  $t \sim 100M_\odot$ . After horizon formation convergence is slower, and, in particular, cannot be monitored at the origin, when the black hole (puncture) forms. In order to minimize the numerical uncertainty for our local analysis presented below, we use the highest number of refinement levels and focus on the model G11H (unless otherwise stated).

Fig. 4 shows the baryonic mass conservation, and the  $L_2$  norm of the Hamiltonian constraint  $\|\mathcal{H}\|_2$ . The relative error in the mass conservation is  $\lesssim 10^{-4}$  up to the collapse. At black hole formation the Hamiltonian constraint (and the momentum constraints, not in the figure) shows a maximum. Constraint violations decrease when the grid is refined and the origin better resolved. Additionally, the higher the resolution is, the smaller the constraint violations are. Notably, for the higher resolutions the violation remains below the level of the initial data due to the use of the Z4c formulation.

The horizon mass and angular momentum, as mea-

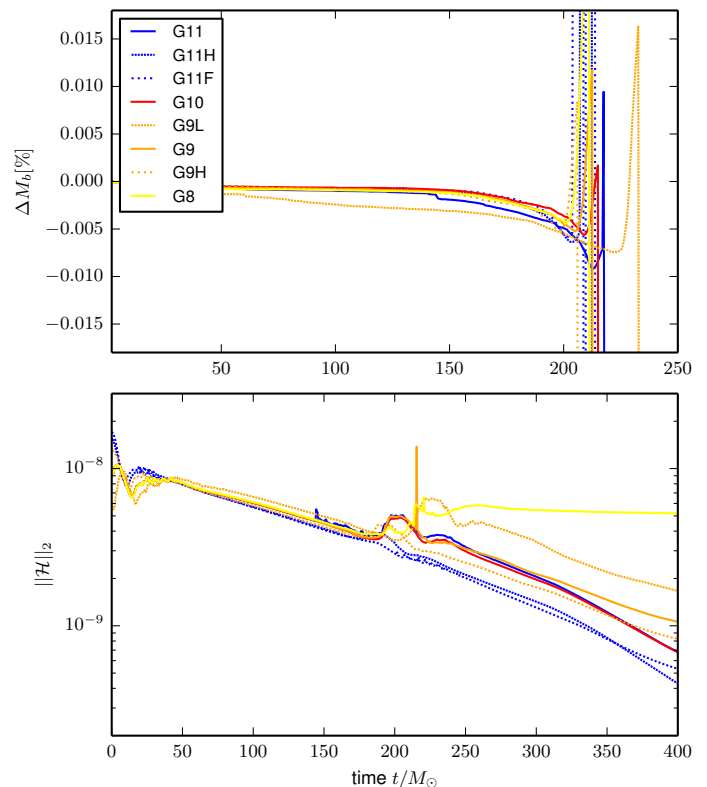


FIG. 4: Rotating collapse dynamics and global quantities: conservation of baryonic mass  $\Delta M_b = 1 - M_b(t)/M_b(0)$  (top),  $L_2$  norm of the Hamiltonian constraint  $\|\mathcal{H}\|_2$  (bottom). The constraint violations are measured on level  $l = 1$ , i.e. the second coarsest level on which the wave extraction also takes place.

sured by the apparent horizon finder, are  $M_{\text{BH}} \sim 1.859(1)M_\odot$  and  $j_{\text{BH}} \sim 0.543(7)$ . In Fig. 5 we show the differences between the horizon mass and spin with respect to the initial ADM quantities and those estimated by the apparent horizon corrected by the amount of energy (angular momentum) emitted in gravitational waves (see below). We find typical relative errors at, or below, the  $\sim 0.1\%$  level.

#### IV. COLLAPSE END STATE

In vacuum, the numerical evolution of puncture black hole initial data [43] approaches an asymptotically cylindrical stationary solution called *trumpet* [44]. The spatial gauge choice, in particular, is responsible for pushing grid points close to the puncture into the black hole interior; the initial wormhole topology ceases to be numerically resolved [45–47]. The end state of a spherical gravitational collapse asymptotically approaches the same trumpet solution found in vacuum simulations [23]. The agreement of end states is again caused by the spatial gauge condition, which allows the matter to fall inwards into a

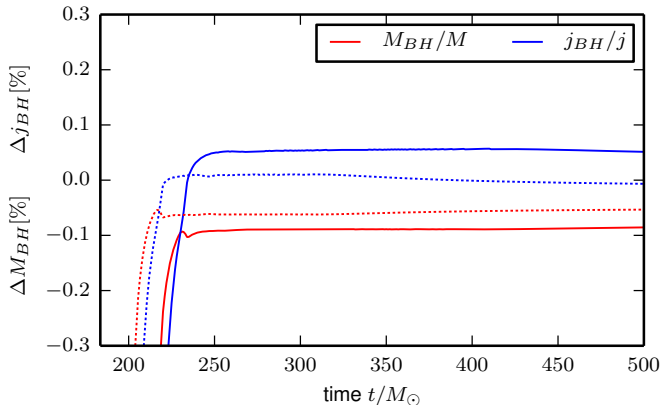


FIG. 5: Differences between the horizon mass (red) and dimensionless angular momentum (blue) of the final black hole corrected by the radiation with respect to the initial ADM quantities of the star. For both quantities the error is below 0.1%. G10 grid data are shown with solid lines; dashed lines are used for G11F data.

region of spacetime that is not resolved by the numerical grid. As stressed in [23], the result is nontrivial because in the collapsing spacetime there is (at least in the matter region) no timelike Killing vector that can lead to a stationary end state, and, at the continuum level, it has different topology than the puncture. Trumpet solutions are also found in dust and gravitational wave collapse [48, 49]. In axisymmetric vacuum spacetimes, one can argue that puncture initial data evolve towards some stationary trumpet slices of Kerr [24, 25, 50–52]. In [24] a first numerical examination of spinning black holes with the puncture gauge was performed and, recently, Ref. [25] found an analytical description of particular trumpet slices in the Kerr spacetime. Our discussion builds on the results of [24].

In the following we demonstrate that the end state of a rotating, collapsing neutron star is a spinning puncture of mass  $M$ . We propose two arguments for this statement; both arguments rely on the fact that various metric functions *at the puncture* can deliver information about the puncture’s spin [24]. In particular, the leading-order behavior of the (square root of the) conformal factor and of the lapse function is

$$\sqrt{\chi}(r \sim 0) \sim c_0 + c_1 r^{\gamma_c}, \text{ and } \alpha(r \sim 0) \sim a_0 + a_1 r^{\gamma_a}, \quad (4)$$

with  $\gamma_c$  and  $\gamma_a$  characteristic exponents that depend on the spin (see Fig. 2 of [24] and Fig. 6 below). Furthermore, the dimensionless spin  $j$  of a puncture can be estimated as

$$j \simeq \sqrt{1.41789 - 4.71218 \cdot \bar{K}(r=0)}, \quad (5)$$

extracting the value of the extrinsic curvature,  $\bar{K} = \hat{K}/M$ , at point  $r = 0$ . In the following, we verify that the spin estimated in the collapsed spacetime from  $\gamma_c$ ,

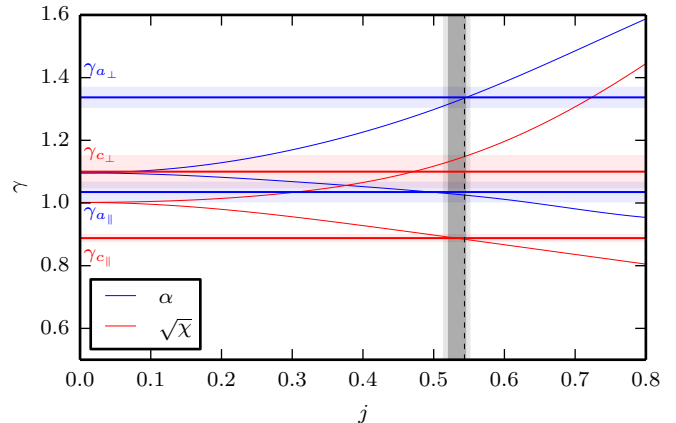


FIG. 6: Characteristic behavior of metric variables  $\sqrt{\chi}$  and  $\alpha$  at  $r = 0$ . Exponents  $\gamma_c$  and  $\gamma_{a,c}$  are extracted by fitting to Eq. (6) for G11H. The thin solid lines are spinning puncture data [24]. The thick lines are collapse data with error bars obtained from our simulations. Red (blue) color refers to  $\chi$  ( $\alpha$ ). The dashed vertical line indicates the angular momentum from the apparent horizon finder. The dark shaded region represents the spin obtained from Eq. 5, the light shaded region the estimate according to  $\gamma_{a,c}$ .

$\gamma_a$ , and  $\bar{K}(r = 0)$  agrees with the angular momentum measured from the apparent horizon.

The exponents  $\gamma_c$  and  $\gamma_a$  can be determined as best fits of the simulation data according to the models, e.g.

$$\sqrt{\chi}(r \sim 0) = c_0 + c_1 r^{\gamma_c} (1 + c_2 r + c_3 r^2) \quad (6)$$

and similarly for the  $\alpha(r \sim 0)$ . The fit is calculated on the radial interval  $r \in [0.01, 0.3]$  in a direction either parallel or perpendicular to the rotational axis ( $z$ -axis). Note that the parallel and perpendicular values actually differ [24]. The results are reported in Fig. 6. The thin solid lines are spinning puncture data in the parallel and perpendicular direction. The straight thick lines are collapse data with error bars estimated with the help of different resolutions and different fitting intervals for  $r$ . Red (blue) color refers to  $\chi$  ( $\alpha$ ). The vertical line indicates the dimensionless angular momentum estimated from the collapse simulation’s apparent horizon. The figure shows that the spinning puncture lines cross the collapse data at these points. The dimensionless angular momentum is compatible with the one of a puncture of the same mass.

Let us also consider a second estimate of the dimensionless spin based on the evolution variables and the puncture gauge. According to [24] the extrinsic curvature depends on the angular momentum of the black hole, when a stationary state is reached. The value  $\bar{K}(r = 0) = \hat{K}(r = 0) \cdot M$  can be extrapolated from a linear fit of  $\hat{K}$  in the region  $r \in [0.05; 0.25]$ . We use an extrapolation perpendicular, orthogonal, and in an angle of  $45^\circ$  to the spin axis. In principle all these values coincide [24]. We receive  $K(r = 0) = 0.1301$  along the  $x$ -axis,  $K(r = 0) = 0.1284$  along the  $z$ -axis, and

$K(r=0) = 0.1293$  along the diagonal for the G11H setup. Using Eq. (5) we get  $j = 0.533 \pm 0.014$ , which agrees with the measured horizon spin within the measurement uncertainty (which is obtained from different resolutions and fitting intervals).

## V. GRAVITATIONAL WAVEFORMS

Gravitational waves are computed by multipole decomposition of the curvature invariant  $r\Psi_4$ ; metric multipoles  $rh_{\ell m}$  are then reconstructed from curvature multipoles (see below). In the following, we discuss both curvature and metric waveforms. Most of the GW energy  $E_{gw} \sim 7.5 \cdot 10^{-7}$  is emitted in the  $(\ell, m) = (2, 0)$  channel. The second dominant mode is the  $(\ell, m) = (4, 0)$  multipole, but, as we shall see, it cannot be computed accurately. We plot waveforms against a retarded time defined as  $u = t - r_* = t - r - 2M \log(r/2M - 1)$ .

Figure 7 shows the two dominant axisymmetric modes  $\ell = 2, 4$  of the curvature waveform. The left panel plots the quadrupolar  $\ell = 2$  mode, which is characterized by a burst of radiation peaking *before* black hole formation and followed by a ringdown pattern. We also show the  $|\Psi_{4(20)}|$  in log scale to highlight the quasinormal ringing phase. According to the ten local maxima between  $u \in [225M_\odot, 380M_\odot]$ , we calculate the fundamental complex frequencies and find  $M\omega = (0.425, -0.0842)$ . Comparing our results with [53] we see that our values agree within (10%, 3%) with perturbation theory [53] assuming  $j = j_{\text{BH}} = 0.544$  and stationarity. (Notice the spacetime in the simulation is still very dynamical at  $t \sim 225M_\odot$ .)

The left panel of Fig. 7 compares our data with those of [13], extracted at scri and kindly provided by the authors. Waveforms are shifted in time to match the peaks. The comparison indicates a very good agreement [66]. Notice that, as in our work, [13] also uses a conservative mesh refinement algorithm, but employs the BSSN-evolution system [54–56] and wave extraction is performed with the Cauchy-characteristic extraction.

As one can observe from the figure’s right panel, the  $\ell = 4$ -mode has amplitude  $\sim 50$  times smaller than the  $\ell = 2$ . The amplitude is of the same order as the burst of radiation caused by the initial (constraint violating) perturbation at early times. These kinds of data are inaccurate, and should be discarded in a physically meaningful analysis.

A self-convergence test on the  $(\ell, m) = (2, 0)$  waveform is shown in Fig. 8. We observe approximate second-order convergence in the G11 data. However, clear pointwise convergence of the waveform is difficult to obtain: since we evolve constraint violating initial data, simulations at different resolutions are inconsistent, and for instance, they do not tend to the same continuum collapse time. Although the effect is rather small, it is visible in the convergence plot as a dephasing in the differences. The effect is larger at lower resolutions (and for larger initial perturbations, not discussed here), but persists also at

high resolutions. We expect it can be removed only by using constraint satisfying initial data.

Further, we study uncertainties due to finite radius extraction. Waveforms computed at different radii  $r = (100, 150, 200, 250, 300)$  and plotted against  $u$  slightly differ in amplitude. A linear extrapolation to  $r \rightarrow \infty$  of  $r\Psi_{420}(u; r)$  shows that the amplitude uncertainty can be as large as 15% for  $r = 100$  and drop to below 5% for  $r = 300$ . This uncertainty can be of the same order of truncation errors. Notice in this comparison the use of the retarded time as defined above in terms of  $r_*$  is essential in order to properly align the waveforms, i.e. the logarithm term  $2M \log(r/2M - 1)$  has a significant contribution at these radii.

Let us turn now to the metric waveform, and discuss its physical features. The multipoles  $h_{\ell m}$  are reconstructed by integrating the relation  $\Psi_4 = \dot{h}$ . We adopt a time domain integration subtracting a quadratic polynomial as described in [57, 58]. Alternatively we have experimented with the frequency domain integration of [59], but in the collapse problem it is difficult to identify a cutting frequency for the high-pass filter proposed there. In both cases the reconstruction introduces inaccuracies in the ringdown.

The dominant mode of the metric waveform is shown in Fig. 9. As pointed out in [1, 26–28], the quadrupole waveform is particularly simple, and characterized by the “precursor-burst-ringdown” pattern well known from black hole perturbation theory (either scattering [60, 61] or radially infalling particles [2, 29, 62, 63]). The figure shows, together with our numerical relativity calculation, the  $\ell = 2$  waveform obtained by a perturbative Gaussian scattering experiment onto a Kerr black hole with  $j = j_{\text{BH}} \sim 0.544$  [64]. The amplitude is scaled by an arbitrary factor. The similarity of the numerical and perturbative waveforms reflects the basic mechanism of the emission process.

It is interesting to connect the waveform features with the collapse dynamics. In perturbation theory this is done, for instance, analyzing the background potential that drives the particle motion [29, 62]. For the collapse dynamics of our study we use the spacetime diagrams of Fig. 1 and connect the dynamics to the emission using the retarded time  $u = t - r_*$ , i.e. using null geodesic of Schwarzschild spacetime. With these assumptions, the events marked in Fig. 1 with horizontal lines correspond to the waveform features marked in Fig. 9. The minimum in the precursor corresponds to time  $t \sim 80M_\odot$ , at which the collapse actually sets in. The first maximum is related to the moment of time at which fluid particles significantly accelerate, and is slightly antecedent apparent horizon formation. Indeed, we find that taking a worldline  $r(t)$  of Fig. 1, the quadrupole waveform  $Q_{20} \propto \ddot{I}_{20} \propto -2\dot{r}^2 - 2r\ddot{r}$ , captures all the qualitative features up to horizon formation. The first maximum in particular is determined by the competitive effect of the two terms in the quadrupole formula:  $-\dot{r}^2 < 0$  and  $-r\ddot{r} > 0$ . At times  $t < 150M_\odot$  the second term domi-

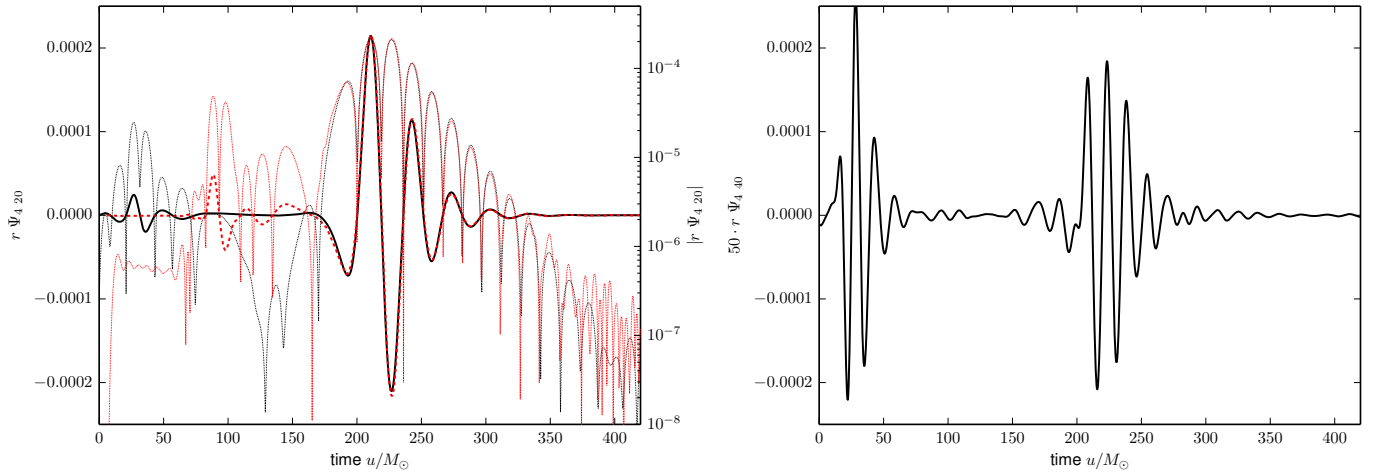


FIG. 7: Rotating collapse curvature waveform  $r\Psi_{\ell m}$  for the dominant multipoles  $(\ell, m) = (2, 0), (4, 0)$ . Left: The  $(\ell, m) = (2, 0)$  mode is shown in linear scale (solid lines) and its modulus in log scale (dotted lines) to highlight the ringdown. The waveform of [13] is shown in red for comparison. Right: The  $(\ell, m) = (4, 0)$  mode is not well resolved by the simulation.

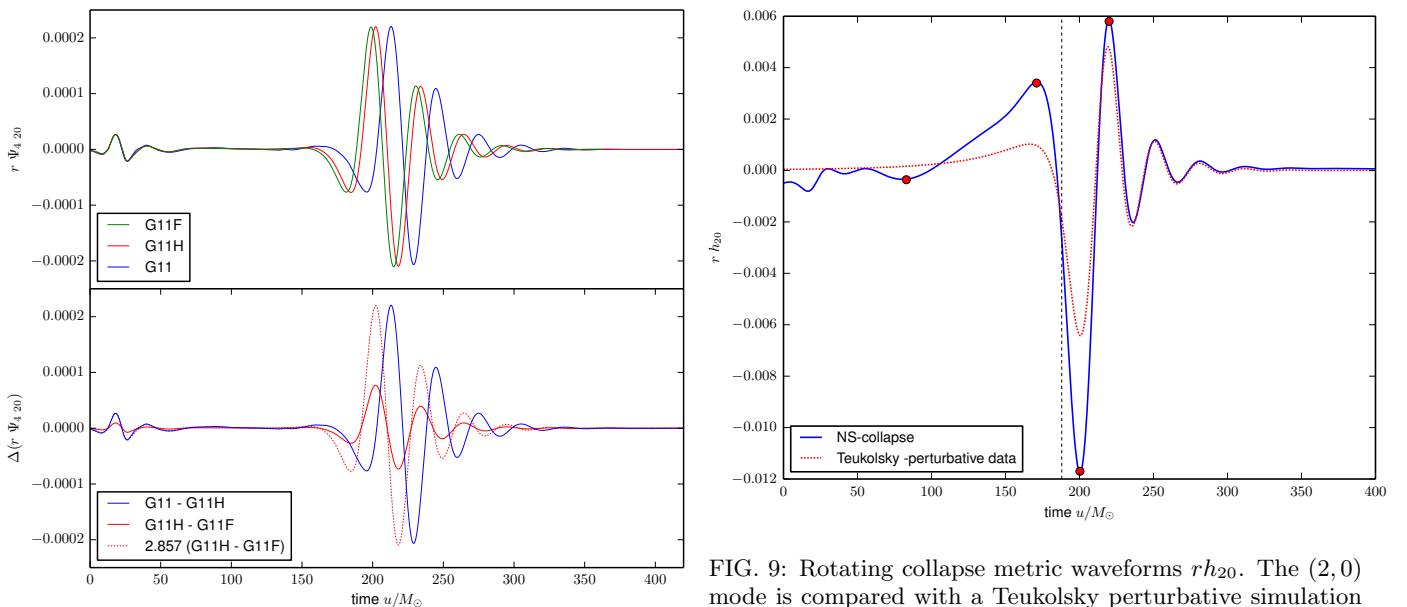


FIG. 8: Rotating collapse curvature waveform  $r\Psi_{4,20}$ , convergence study.

nates,  $-r\ddot{r} > \dot{r}^2$ , but at later times  $t > 150M_\odot$  the first (velocity) term becomes comparable  $\dot{r}^2 \sim -r\ddot{r}$ . The maximum in the wave at  $t \sim 175M_\odot$  results from the growth of  $\dot{r}^2$ ; the zero crossing at  $t \sim 180M_\odot$  marks the instantaneous balance between the two terms. The metric waveform has its absolute minimum *shortly after* black hole formation (see dashed vertical line in Fig. 1), when the mass enclosed by the horizon is  $M_{\text{BH}} \sim M$  and its radius is approximately constant. The metric waveform peaks *after* black hole formation when all the matter is inside the horizon and the black hole rings down.

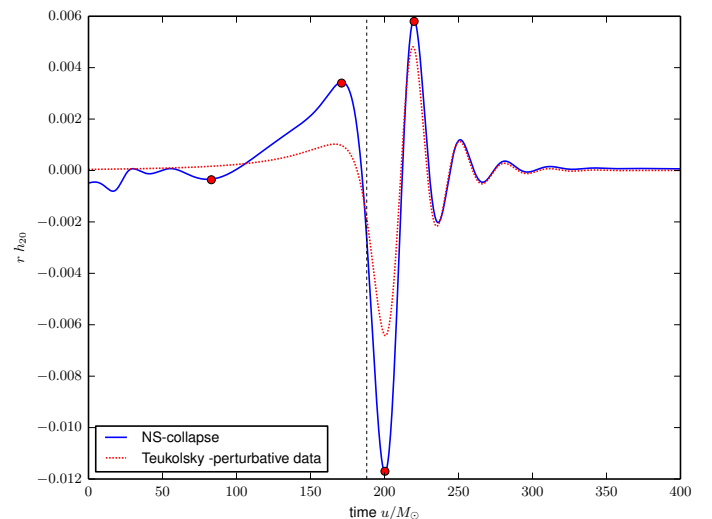


FIG. 9: Rotating collapse metric waveforms  $r h_{20}$ . The  $(2, 0)$  mode is compared with a Teukolsky perturbative simulation of black hole scattering; see text for details. The waveform main features are marked with red dots and correspond to the events (horizontal lines) in Fig. 1. The horizon formation is marked with a vertical dashed line.

## VI. SUMMARY

Puncture gauge conditions play a key role in the simulations of rotational collapse as they “automatically” handle the singularity formation and subsequent evolution [22, 23]. Building on previous work and extending it, we have demonstrated that the end state of an axisymmetric collapse in the puncture gauge is the same as the one obtained from the evolution of a spinning puncture [24]. Our statement refers to a simple and controlled



case study (an unstable uniformly rotating equilibrium configuration perturbed to collapse) but the result holds for generic simulations in which the puncture gauge is employed. For instance, rotational collapse characterizes the end phase of certain binary neutron star configurations or supernova core collapse. Not surprising, the same arguments used in this paper can be applied to those data, e.g. [24] for preliminary results.

Our results strongly rely on the precision of the presented simulations. In particular, we have used a conservative mesh refinement scheme for the hydrodynamics evolution [13, 31, 32] which allowed us to refine the star and increase the resolution near the center (puncture) without mass losses. Also, we have employed the Z4c formulation of Einstein equations, which improves accuracy and constraint preservation in a free evolution (hyperbolic) approach to general relativity [33, 34].

The calculation of gravitational waves is particularly sensitive to numerical resolution and errors. In these simulations, the waveform quality can be corrupted by spurious radiation related to constraint violations. Our data agree with the recent work of [13]; some earlier three-dimensional calculations appear as affected by unphysical features probably due to low resolution employed and the high initial perturbation. The collapse waveform is rather simple and qualitatively similar (“precursor-burstingdown”) to those from black hole perturbation theory [1, 28, 29]. Using the spacetime diagram of Fig. 1,

we have identified and connected all its main features to precise stages of the collapse dynamics.

## Acknowledgments

The authors thank Christian Reisswig and Christian Ott for discussions and for providing the waveform used in Fig. 7; Enno Harms for providing the data of the Teukolsky perturbative simulation used in Fig. 9; Bernd Brügmann, Alessandro Nagar, Pedro Montero, and Nicolas Sanchis-Gual for discussions; and Nathan Johnson-McDaniel for comments on the manuscript. This work was supported in part by DFG grant SFB/Transregio 7 “Gravitational Wave Astronomy” and the Graduierten-Akademie Jena. S.B. acknowledges partial support from the National Science Foundation under Grants No. NSF AST-1333520, No. PHY-1404569, and No. AST-1205732. The authors acknowledge the Gauss Centre for Supercomputing e.V. for providing computing time on the GCS Supercomputer SuperMUC (Munich), the John von Neumann Institute for Computing (NIC) providing computing time of JUROPA (JSC), and the Extreme Science and Engineering Discovery Environment (XSEDE) for providing computer time on Stampede (Texas).

- 
- [1] R. Stark and T. Piran, *Phys.Rev.Lett.* **55**, 891 (1985).
  - [2] T. Nakamura, K. Oohara, and Y. Kojima, *Prog. Theor. Phys. Suppl.* **90**, 1 (1987).
  - [3] M. Shibata, *Phys. Rev.* **D67**, 024033 (2003), gr-qc/0301103.
  - [4] M. D. Duez, Y. T. Liu, S. L. Shapiro, M. Shibata, and B. C. Stephens, *Phys. Rev. Lett.* **96**, 031101 (2006), astro-ph/0510653.
  - [5] M. Shibata, M. D. Duez, Y. T. Liu, S. L. Shapiro, and B. C. Stephens, *Phys. Rev. Lett.* **96**, 031102 (2006), astro-ph/0511142.
  - [6] B. C. Stephens, M. D. Duez, Y. T. Liu, S. L. Shapiro, and M. Shibata, *Class.Quant.Grav.* **24**, S207 (2007), gr-qc/0610103.
  - [7] B. C. Stephens, S. L. Shapiro, and Y. T. Liu, *Phys. Rev.* **D77**, 044001 (2008), 0802.0200.
  - [8] M. Shibata, T. W. Baumgarte, and S. L. Shapiro, *Phys.Rev.* **D61**, 044012 (2000), astro-ph/9911308.
  - [9] M. D. Duez, S. L. Shapiro, and H.-J. Yo, *Phys.Rev.* **D69**, 104016 (2004), gr-qc/0401076.
  - [10] L. Baiotti, I. Hawke, P. J. Montero, F. Löffler, L. Rezzolla, et al., *Phys.Rev.* **D71**, 024035 (2005), gr-qc/0403029.
  - [11] L. Baiotti, I. Hawke, and L. Rezzolla, *Class. Quant. Grav.* **24**, S187 (2007), gr-qc/0701043.
  - [12] B. Giacomazzo, L. Rezzolla, and N. Stergioulas, *Phys.Rev.* **D84**, 024022 (2011), 1105.0122.
  - [13] C. Reisswig, R. Haas, C. Ott, E. Abdikamalov, P. Mösta, et al., *Phys.Rev.* **D87**, 064023 (2013), 1212.1191.
  - [14] C. Ott, C. Reisswig, E. Schnetter, E. O’Connor, U. Sperhake, et al., *Phys.Rev.Lett.* **106**, 161103 (2011), 1012.1853.
  - [15] M. Thierfelder, S. Bernuzzi, and B. Brügmann, *Phys.Rev.* **D84**, 044012 (2011), 1104.4751.
  - [16] N. Andersson, J. Baker, K. Belczynski, S. Bernuzzi, E. Berti, et al., *Class.Quant.Grav.* **30**, 193002 (2013), 1305.0816.
  - [17] C. Bona, J. Massó, E. Seidel, and J. Stela, *Phys. Rev. Lett.* **75**, 600 (1995), gr-qc/9412071.
  - [18] M. Alcubierre, B. Brügmann, P. Diener, M. Koppitz, D. Pollney, E. Seidel, and R. Takahashi, *Phys. Rev. D* **67**, 084023 (2003), gr-qc/0206072.
  - [19] J. R. van Meter, J. G. Baker, M. Koppitz, and D.-I. Choi, *Phys. Rev. D* **73**, 124011 (2006), gr-qc/0605030.
  - [20] M. Campanelli, C. O. Lousto, P. Marronetti, and Y. Zlochower, *Phys. Rev. Lett.* **96**, 111101 (2006), gr-qc/0511048.
  - [21] J. G. Baker, J. Centrella, D.-I. Choi, M. Koppitz, and J. van Meter, *Phys. Rev. Lett.* **96**, 111102 (2006), gr-qc/0511103.
  - [22] L. Baiotti and L. Rezzolla, *Phys. Rev. Lett.* **97**, 141101 (2006), gr-qc/0608113.
  - [23] M. Thierfelder, S. Bernuzzi, D. Hilditch, B. Brügmann, and L. Rezzolla, *Phys.Rev.* **D83**, 064022 (2011), 1012.3703.
  - [24] T. Dietrich and B. Brügmann, *J.Phys.Conf.Ser.* **490**, 012155 (2014), 1403.5746.
  - [25] K. A. Dennison, T. W. Baumgarte, and P. J. Montero,



- Phys.Rev.Lett. **113**, 261101 (2014), 1409.1887.
- [26] E. Seidel and T. Moore, Phys.Rev. **D35**, 2287 (1987).
  - [27] E. Seidel, E. Myra, and T. Moore, Phys.Rev. **D38**, 2349 (1988).
  - [28] E. Seidel, Phys. Rev. **D42**, 1884 (1990).
  - [29] M. Davis, R. Ruffini, W. Press, and R. Price, Phys.Rev.Lett. **27**, 1466 (1971).
  - [30] B. Giacomazzo and R. Perna, Astrophys.J. **758**, L8 (2012), 1209.0783.
  - [31] M. J. Berger and P. Colella, Journal of Computational Physics **82**, 64 (1989).
  - [32] W. E. East, F. Pretorius, and B. C. Stephens, Phys.Rev. **D85**, 124010 (2012), 1112.3094.
  - [33] S. Bernuzzi and D. Hilditch, Phys. Rev. **D81**, 084003 (2010), 0912.2920.
  - [34] D. Hilditch, S. Bernuzzi, M. Thierfelder, Z. Cao, W. Tichy, et al., Phys. Rev. **D88**, 084057 (2013), 1212.2901.
  - [35] A. Weyhausen, S. Bernuzzi, and D. Hilditch, Phys. Rev. **D85**, 024038 (2012), 1107.5539.
  - [36] J. A. Font, Living Rev. Rel. **11**, 7 (2007).
  - [37] B. Brügmann, J. A. Gonzalez, M. Hannam, S. Husa, U. Sperhake, et al., Phys.Rev. **D77**, 024027 (2008), gr-qc/0610128.
  - [38] M. J. Berger and J. Olinger, J.Comput.Phys. **53**, 484 (1984).
  - [39] R. Borges, M. Carmona, B. Costa, and W. S. Don, Journal of Computational Physics **227**, 3191 (2008).
  - [40] S. Bernuzzi, A. Nagar, M. Thierfelder, and B. Brügmann, Phys.Rev. **D86**, 044030 (2012), 1205.3403.
  - [41] T. Dietrich, S. Bernuzzi, M. Ujevic, and B. Brügmann (2015), 1504.01266.
  - [42] N. Stergioulas and J. L. Friedman, Astrophys. J. **444**, 306 (1995), astro-ph/9411032.
  - [43] S. Brandt and B. Brügmann, Phys. Rev. Lett. **78**, 3606 (1997), gr-qc/9703066.
  - [44] M. Hannam, S. Husa, D. Pollney, B. Brügmann, and N. O’Murchadha, Phys. Rev. Lett. **99**, 241102 (2007), gr-qc/0606099.
  - [45] J. D. Brown, Phys. Rev. **D77**, 044018 (2008), 0705.1359.
  - [46] D. Garfinkle, C. Gundlach, and D. Hilditch, Class. Quant. Grav. **25**, 075007 (2008), 0707.0726.
  - [47] M. Hannam, S. Husa, F. Ohme, B. Brügmann, and N. O’Murchadha, Phys.Rev. **D78**, 064020 (2008), 0804.0628.
  - [48] A. Staley, T. Baumgarte, J. Brown, B. Farris, and S. Shapiro, Class.Quant.Grav. **29**, 015003 (2012), 1109.0546.
  - [49] D. Hilditch, T. W. Baumgarte, A. Weyhausen, T. Dietrich, B. Brügmann, P. J. Montero, and E. Müller, Phys.Rev. **D88**, 103009 (2013), 1309.5008.
  - [50] M. Hannam, S. Husa, and N. O. Murchadha, Phys.Rev. **D80**, 124007 (2009), 0908.1063.
  - [51] M. E. Gabach Clement, Class.Quant.Grav. **27**, 125010 (2010), 0911.0258.
  - [52] S. Dain and M. E. Gabach Clement, Class.Quant.Grav. **26**, 035020 (2009), 0806.2180.
  - [53] E. Berti, V. Cardoso, and A. O. Starinets, Class. Quant. Grav. **26**, 163001 (2009), 0905.2975.
  - [54] T. Nakamura, K. Oohara, and Y. Kojima, Prog. Theor. Phys. Suppl. **90**, 1 (1987).
  - [55] M. Shibata and T. Nakamura, Phys. Rev. **D52**, 5428 (1995).
  - [56] T. W. Baumgarte and S. L. Shapiro, Phys. Rev. **D59**, 024007 (1998), gr-qc/9810065.
  - [57] T. Damour, A. Nagar, M. Hannam, S. Husa, and B. Brügmann, Phys. Rev. **D78**, 044039 (2008), 0803.3162.
  - [58] L. Baiotti, S. Bernuzzi, G. Corvino, R. De Pietri, and A. Nagar, Phys. Rev. **D79**, 024002 (2009), 0808.4002.
  - [59] C. Reisswig and D. Pollney, Class.Quant.Grav. **28**, 195015 (2011), 1006.1632.
  - [60] C. V. Vishveshwara, Nature **227**, 936 (1970).
  - [61] S. Bernuzzi, A. Nagar, and R. De Pietri, Phys. Rev. **D77**, 044042 (2008), 0801.2090.
  - [62] M. Davis, R. Ruffini, and J. Tiomno, Phys. Rev. **D5**, 2932 (1972).
  - [63] C. O. Lousto and R. H. Price, Phys.Rev. **D55**, 2124 (1997), gr-qc/9609012.
  - [64] E. Harms, S. Bernuzzi, A. Nagar, and A. Zenginoglu, Class.Quant.Grav. **31**, 245004 (2014), 1406.5983.
  - [65] The puncture gauge is effectively used within the moving puncture approach introduced in [20, 21].
  - [66] The  $\Psi_4$  20 waveform visually agrees also with the one of [30].